

Boron From Net Charge Acceptor to Donor and Its Effect on Hydrogen Uptake by Novel Mg-B-electrochemically Synthesized Reduced Graphene Oxide

Satya Aditya Marla

Indian Institute of Technology Bombay

Srikanta Panda

Indian Institute of Technology Bombay

Sankara Sarma Tatiparti (✉ sankara@iitb.ac.in)

Indian Institute of Technology Bombay

Research Article

Keywords: Boron, Mg-B-electrochemically, Graphene Oxide

Posted Date: November 24th, 2020

DOI: <https://doi.org/10.21203/rs.3.rs-109421/v1>

License: © ⓘ This work is licensed under a Creative Commons Attribution 4.0 International License.

[Read Full License](#)

Abstract

Hydrogen uptake (H-uptake) is studied in ball milled Mg-B-electrochemically synthesized reduced graphene oxide (erGO) nanocomposites at $P_{H_2} \approx 15$ bar, ~ 320 °C. B/C (weight ratio): 0, ~ 0.09 , ~ 0.36 , ~ 0.90 are synthesized maintaining erGO ≈ 10 wt %. B occupies octahedral interstices within Mg unit cell - revealed by electron density maps. Persistent charge donations from Mg and B to C appear as Mg-C (~ 283.2 eV), B-C (~ 283.3 - 283.9 eV) interactions in C-1s core X-ray photoelectron spectrometry (XPS) at all B/C . At $B/C > 0.09$, charge reception by B from Mg yields Mg-B interaction (51.3 eV, Mg-2p XPS). This net charge acceptor role of B does not alter Mg unit cell size significantly. Despite charge donation to both C and B, the Mg charge is $< +2$, resulting in long incubation times (> 5 h) at $B/C > 0.09$. In $B/C \approx 0.09$, C-2p $\pi \rightarrow \pi^*$ transition (~ 290 eV, C-1s XPS) is also seen. Absence of Mg-B interaction renders B a charge donor, resulting in Mg-B repulsion and Mg unit cell expansion. Mg-C peak shift to lower binding energies (C-1s XPS), decreases incubation time to 2.25 h and increases H-uptake kinetics. Various atomic interactions influence the reduction of incubation time in H-uptake and increase its kinetics in the order: $(Mg \rightarrow C; B \rightarrow C)_{B/C \approx 0.09} > (Mg \rightarrow C)_{B/C = 0} > (\text{ternary } Mg \rightarrow B \rightarrow C)_{B/C > 0.09}$.

Introduction

Magnesium (hydride) is a promising material for hydrogen storage due to its high gravimetric capacity (~ 7.6 wt %) and its abundance (as oxide)¹. However, its poor kinetics of hydrogen uptake (H-uptake) and release pose significant challenges for its use as on-board hydrogen storage material for automobile applications^{2,3}. H-uptake by Mg suffers from the presence of incubation time during which Mg cannot absorb any hydrogen⁴. For example, Mg failed to hydrogenate at $P_{H_2} = 10$ bar and 300 °C⁴. At 400 °C, H-uptake started only after 30 minutes of the commencement of the experiment⁴.

Nanosizing and catalyst addition can enhance the H-uptake/release kinetics significantly^{5,6}. In a study, decreasing the particle size of MgH_2 to ~ 12 nm by ball milling resulted in a four-fold decrease in the H-uptake/release time at $P_{H_2} \approx 0.1$ bar and ~ 350 °C⁷. For on-board hydrogen storage applications, the weight of the material needs to be kept minimal. The light weight, 2-dimensional carbon based materials such as reduced graphene oxide (rGO) are widely studied as catalysts, supports and confining agents⁸. They can enhance kinetics, and inhibit the agglomeration and surface oxidation of the nanosized $Mg(H_2)$ particles⁹. In a recent study, Liu et al.¹⁰ reported that 5 wt % of rGO can result in the desorption of ~ 6.3 wt % hydrogen from MgH_2 in 80 minutes. Boron (B), which is even lighter than C, can also catalyze H-release in Mg-based materials. However, mostly, its catalytic effects have been realized only indirectly. For example, $Mg(BH_4)_2$ renders H-release in stages with the formation of an intermediate compound ($MgB_{12}H_{12}$) and accelerates the desorption process upon in-situ MgB_2 formation¹¹. This in-situ formation of MgB_2 occurs even during desorption from hydride mixtures such as $LiBH_4$ - MgH_2 and catalyzes H-release by MgH_2 ¹². Theoretical studies on B inclusion in MgH_2 reported lattice changes and increase in H-H distance¹³. Binary Mg-B, B-rGO and Mg-rGO systems were studied in the past^{9,10,14-16}. B-doped

graphene improves enthalpy of H-release in MgH_2 ¹⁷. Nevertheless, the investigations on $\text{Mg}(\text{H}_2)$ -B-rGO ternary system are in their early stages, particularly during H-uptake. Moreover, the charge transfer role of B and its impact on the hydrogen storage by Mg-rGO system are not well known from literature.

Most of the studies on hydrogen storage by MgH_2 -based materials are focussed on H-release rather than H-uptake. Some scientific reasons for this are (i) uncertainty involved in experimentally identifying the lattice positions of H, any elemental additions etc. in the crystalline hydrogen-hosts upon H-uptake; this further renders (ii) the investigation of various atomic interactions among the components difficult; (iii) such uncertainties in structural investigations can lead to erroneous estimation of enthalpy and entropy changes – This is particularly true in the case of composite systems such as $\text{Mg}(\text{H}_2)$ -B-rGO, where both Mg and C (from rGO) can, synergistically, form bonds with $\text{H}^{9,18}$. Our earlier study on H-uptake and release by Mg-rGO demonstrates that along with Mg, C also forms bond with H due to charge (electron) transfer from Mg to C^{18} . Practically, the H-uptake studies are less appealing than their H-release counterparts for reporting, since H-uptake involves long incubation times⁴. Nevertheless, hydrogen storage involves both H-uptake and release and the studies on the former are indispensable.

In the present study H-uptake by the novel Mg-B-erGO nanocomposites at $P_{\text{H}_2} \approx 15$ bar and ~ 320 °C is reported. The erGO is a novel electrochemically synthesized rGO, which we reported in our recent study, that contains fewer functional groups than rGO prepared by the modified Hummer's method¹⁹. Here, Mg, B and erGO are ball milled together at various B/C weight ratios (0, ~ 0.09 , ~ 0.36 and ~ 0.90) maintaining 10 wt % of erGO in the nanocomposites. Several interactions among Mg, B and C, involving charge transfer, develop upon ball milling. Interestingly, a "critical" B/C ratio (~ 0.09) is identified. Below this ratio B is a charge (electron) donor to C. Above this ratio B accepts charge from Mg and also donates to C, acting as a net charge acceptor. When B is charge donor, a decrease in the incubation time is observed for H-uptake from ~ 3.25 h in the absence of B to ~ 2.25 h (i.e. a drop of $\sim 31\%$) upon slight addition of B ($B/C \approx 0.09$). Various fundamental scientific questions are answered: (i) How and why does B affect the Mg unit cell? (ii) How and why do interactions among Mg, B and C develop? (iii) Why does B switch the role from charge donor to net acceptor upon increasing its content? (iv) What is the impact of this role-switching by B on the H-uptake by the Mg-B-erGO nanocomposites? Our claims are supported by X-ray diffraction (XRD), X-ray photoelectron spectroscopy (XPS) (C-1s, Mg-2p and B-1s spectra) and the novel electron density maps, the technique which we used elsewhere²⁰.

Results

Incubation time during H-uptake

The H-uptake by all the Mg-B-erGO nanocomposites at $P_{\text{H}_2} \approx 15$ bar and ~ 320 °C is plotted as wt % hydrogen in Mg versus time in Fig. 1. For all the nanocomposites, an incubation time corresponding to negligible H-uptake was seen before initiation of hydrogen absorption. These incubation times are plotted as function of B/C ratio in the inset of Fig. 1. The incubation time decreases from ~ 3.25 h in $B/C=0$ to

~2.25 h with a slight addition of B ($B/C \approx 0.09$). Surprisingly, with further addition of B the nanocomposites exhibit increased incubation time (inset, Fig. 1). This clearly indicates that there is a critical B/C ratio at which the incubation time reaches a minimum. Here, 0.09 is taken as the critical B/C ratio. It can also be seen that, following the incubation time all the H-uptake curves are sigmoidal in nature, prior to reaching saturation levels at ~6 wt %. The rate of H-uptake is the highest at the critical B/C . The nanocomposite with $B/C \approx 0.90$ has the lowest rate of uptake and the longest incubation time. Figure 1 suggests that B plays a role in governing the incubation time and the kinetics of H-uptake by these nanocomposites.

Phase analysis

The X-ray diffraction (XRD) patterns of the ball milled nanocomposites (Supplementary Fig. S1) indicate the presence of hexagonal close packed (hcp) Mg. The XRD patterns also show the presence of MgO, indicating oxidation of Mg⁹. The oxygen from the functional groups present in erGO sheets released while ball milling could have reacted with Mg²¹. Also, any possible mild exposure to air while transporting the nanocomposites could also have resulted in the formation of MgO. The phase percentages of Mg and MgO (Supplementary Table S1) were estimated from XRD patterns through Rietveld refinement using FullProf suite (version: 7.20)²². The crystallite size of Mg in all the ball milled nanocomposites is ~24 nm from Scherrer equation²³. The XRD pattern of the erGO is shown in Supplementary Fig. S2.

Structural changes in Mg unit cell

Figure 2 shows the lattice parameters of the Mg unit cell, estimated from XRD patterns through Rietveld refinement using FullProf suite (version: 7.20)²². Prior to analyzing the obtained lattice parameters, the structural integrity of the crystal for all the nanocomposites was verified and ensured by noting that the c/a ratio is almost constant and is close to the theoretical value of 1.623 for an hcp crystal²⁴ (inset, Fig. 2). Both a and c increase with an increase in the B/C ratio from 0 to ~0.09, indicating the Mg lattice expansion. With further increase in B/C to ~0.36 both a and c decrease, resulting in shrinkage of Mg lattice. At the highest B/C (~0.90), the a and c show only negligible change with respect to B/C of 0 and ~0.36.

Local environment in Mg unit cell

The local environment in the Mg unit cell is estimated by developing the electron density maps²⁵ for the $(\bar{1}0 - \bar{1}0)$ plane intersecting the atom 'Mg1' as shown in Fig. 3a. The colour-coded scales adjacent to the maps in Fig. 3a represent the electron density $\rho(r)$ (= number of electrons/volume (\AA^{-3})) values. It is to be noted that the positive value in these scales correspond to the presence of electrons and the negative values correspond to their absence. All the maps in Fig. 3a show that the maximum electron density is present in the regions, where the Mg atoms are located. This indicates the concentration of the maximum number of electrons around Mg. A careful observation of Fig. 3a suggests that the charge distribution around Mg is not similar in all the nanocomposites. This can be seen by the asphericity of the electron

density distribution around Mg (p/q , Fig. 3a). The asphericity is estimated as the ratio of the distance along b to that along c from the center of Mg up to the outermost position, where the positive electron density can be observed. The estimated asphericities are ~ 1.17 , ~ 1.11 , ~ 0.98 and ~ 1.22 for B/C s of 0, ~ 0.09 , ~ 0.36 and ~ 0.90 , respectively. Therefore, the electron density distribution is nearly uniform (asphericity closer to 1) for the nanocomposites of $B/C \approx 0.09$ and 0.36 . The aspherical charge distribution suggests covalency in Mg²⁰. Figure 3b shows the relative electron density at the octahedral interstices in the (0001) basal plane of the Mg unit cell ('Octahedral interstices', Fig. 3b), normalized with respect to the maximum electron density found around Mg (i.e. $\rho_{\text{Octahedral}}/\rho_{\text{max}}$). The corresponding electron density maps are shown in Supplementary Fig. S3. It is known that the dopants can occupy these sites when incorporated in the Mg unit cell²⁶. A negative value of this relative electron density indicates the absence of electrons and vice versa. The relative electron densities of the nanocomposites with B/C of 0 and ~ 0.90 are negative, mutually comparable, and lie between those of ~ 0.09 (negative) and ~ 0.36 (positive). The nanocomposite with $B/C \approx 0.09$ has the least relative electron density; whereas, it is the highest for $B/C \approx 0.36$. This suggests that among all the nanocomposites the octahedral sites in $B/C \approx 0.09$ are least populated sites for electrons, suggesting a possible presence of a positively charged species.

Chemical interactions

The core C-1s and Mg-2p X-ray photoelectron spectra (XPS) of all the nanocomposites are shown in Fig. 4a and 4b, respectively. The experimental data obtained from XPS were deconvoluted using Gaussian profile to estimate the atomic interactions²⁷. In C-1s spectra, the peaks at the binding energies ~ 283.2 eV, ~ 283.3 - 283.9 eV, ~ 284.6 eV, ~ 285.7 eV, ~ 286.6 eV, and ~ 290 eV correspond to Mg-C¹⁸, B-C^{28,29}, C-C sp², C-OH, C-O-C^{30,31} and C-2p $\pi \rightarrow \pi^*$ transition^{9,32}, respectively. The alcohol (-OH) and epoxy (C-O-C) functional groups arise during the synthesis of erGO (C-1s spectrum of erGO, Supplementary Fig. S4). From Fig. 4a, the Mg-C interactions in $B/C=0$ are seen at ~ 283.2 eV. The deconvoluted spectrum of $B/C \approx 0.09$ shows the B-C peak at ~ 283.5 eV. With further increase in B/C to ~ 0.36 the B-C peak shifted towards higher binding energy. For the highest B/C (≈ 0.90) a slight decrease in the B-C peak position can be seen from Fig. 4a. The Mg-C peaks also show a similar trend with the B/C ratio. The C-2p $\pi \rightarrow \pi^*$ transition peak is visible only in the nanocomposites with B/C of 0 and ~ 0.09 . Interestingly, C-2p $\pi \rightarrow \pi^*$ transition peak is absent in the nanocomposites with higher B/C ratios.

The peaks corresponding to metallic Mg and MgO are seen in all the compositions in Mg-2p XPS spectra (Fig. 4b). The peaks of metallic Mg lie within the binding energy range ~ 47.5 - 49.5 eV³³. The charge of Mg in MgO (<+2) causes an increase in binding energy, as the net number of electrons in the Mg valence shell in MgO are lower than those in metallic Mg³⁴. The binding energy values of MgO in the present study lie within ~ 49 - 51 eV, consistent with literature³⁵. The Mg-B peaks are seen only at higher B/C s (≥ 0.36) and appear around ~ 51.3 eV^{36,37}. The analysis of C-1s and Mg-2p spectra indicates that the signals present at lower B/C s (0, ~ 0.09) are absent at higher B/C s (~ 0.36 , ~ 0.90) and vice versa.

Discussion

The results suggest a critical B/C ratio of ~ 0.09 , at which the incubation time during hydrogen uptake by the Mg-B-erGO nanocomposites is the least and increases above or below this ratio (Fig. 1). The crystallographic (Fig. 2) and local environmental (Fig. 3 and 4) changes with the addition of B are used to understand the reasons behind this observation. The presence of Mg, B and C renders the scenario complex by developing binary Mg-C, Mg-B, B-C and possible ternary Mg-B-C interactions upon ball milling. These interactions can affect the incubation time during H-uptake.

In the nanocomposite where B is absent ($B/C=0$), the covalency of Mg as suggested by the aspherical charge distribution³⁸ (p/q , Fig. 3a) indicates that there is an interaction between Mg and the surroundings. Further, the negative relative electron density in the octahedral interstices of the (0001) basal plane in Mg in $B/C=0$ (Fig. 3b, Supplementary Fig. S3) shows the deficiency of electrons at this site. This suggests that there is no electron donation from Mg to this octahedral site. Therefore, it is reasonable to conclude that Mg donates electrons to C, which appears as 'Mg-C' peak in C-1s XPS spectrum (Fig. 4a). This Mg-C interaction results in the C-2p $\pi \rightarrow \pi^*$ transition peak, which is seen at ~ 290 eV in the C-1s spectrum (Fig. 4a)^{39,40}. This electron donation from Mg to C can be reinforced by the fact that the electronegativity (χ) on the Pauling scale for Mg (~ 1.20) is lower than that for C (~ 2.55)⁴¹. However, it is to be noted that these electronegativity values are applicable when Mg and C are in their pure elemental states. Any local changes in the chemical environment can cause deviation from these electronegativity values. In our earlier work, we demonstrated that the Mg-C interaction causes an increase of charge on carbon atoms leading to a change of hybridization in C from sp^2 to sp^3 , resulting in the C-H bond aiding H-uptake¹⁸.

A slight addition of B in $B/C \approx 0.09$ decreases incubation time and enhances H-uptake kinetics (Fig. 1). This improvement is due to the structural and local environmental changes introduced by B. Upon addition of B, a significant expansion of the Mg unit cell can be seen from the lattice parameters in Fig. 2. Normally, the repulsive forces between two entities within a unit cell can cause its expansion⁴². In the present scenario, it can be expected that B is incorporated within the Mg unit cell and possesses a positive charge. The incorporation of B happens in such a way that the structural integrity of the Mg unit cell is maintained (inset, Fig. 2). The lower asphericity in $B/C \approx 0.09$ compared to that in $B/C=0$ shown in Fig. 3a suggests that the Mg in $B/C \approx 0.09$ is less covalent than that in $B/C=0$ ³⁸. Most likely, the repulsion between the positively charged B and Mg is the reason for this. The relative electron density at the octahedral interstices in the (0001) Mg basal plane of $B/C \approx 0.09$ is more negative with respect to that of $B/C=0$ (Fig. 3b, Supplementary Fig. S3). In other words, the charge in these regions is more positive in $B/C \approx 0.09$ compared with that in $B/C=0$. This change is attributed to the possible presence of positively charged B in these interstices⁴³ in the nanocomposite with $B/C \approx 0.09$. The likely reason for the positive charge over B is the charge transfer from B to Mg and/or to C. However, the charge transfer from B to Mg may not be possible as the electronegativity of elemental B is ~ 2.05 and that of Mg is ~ 1.20 ⁴¹. Therefore,

most likely, the charge transfer takes place from B to C, giving rise to B-C interaction at ~ 283.5 eV (Fig. 4a).

In general, B-C interactions are also possible when B is doped in rGO¹⁹. However, in the present study, the B-1s core spectra for all the nanocomposites (Supplementary Fig. S5), show the absence of peaks corresponding to boron doping in carbon at various positions viz. B substitution at C (~ 189.1 eV), B_4C (~ 187.7 eV), C_2-BO (~ 191.4 eV), $C-BO_2$ (~ 191.8 eV)⁴⁴. This clearly indicates that there is no strong bond formation between B and C in the present study. Along with the B-C peak, C-1s core spectrum (Fig. 4a) also shows both Mg-C and C-2p $\pi \rightarrow \pi^*$ transition peaks at the same positions as those in the case of $B/C=0$. This clearly shows that for the nanocomposite with $B/C \approx 0.09$, the Mg-C interaction and C-2p $\pi \rightarrow \pi^*$ transition are not affected significantly upon B addition. The reason for this is that there is no significant charge transfer between Mg and B in $B/C \approx 0.09$, rendering the Mg-C interaction and C-2p $\pi \rightarrow \pi^*$ transition almost unchanged in this nanocomposite with respect to $B/C=0$. The presence of both Mg-C and B-C interactions in $B/C \approx 0.09$ show that both Mg and B are charge donors to C.

Upon increasing the B content in the nanocomposites to $B/C \approx 0.36$ and 0.90 both the incubation time and the kinetics of H-uptake are deteriorated (Fig. 1). Interestingly, the lattice parameters of these nanocomposites are close to those of $B/C=0$ (Fig. 2). The possible reasons for the restoration of the Mg unit cell to its original size are: (i) B is not present within the Mg unit cell at these compositions; (ii) B is present within the unit cell and shrinks its size to almost the original value by developing possible additional interactions. However, it is likely that B is incorporated in the Mg unit cell even at compositions higher than in $B/C \approx 0.09$ (Fig. 3(b)). Therefore, the first reason is not plausible. Hence, the possible presence of B in the Mg unit cell is maintaining its size closer to its pristine counterpart ($B/C=0$). From Fig. 3a, the charge distribution around Mg atom clearly shows that it is almost spherical for $B/C \approx 0.36$ and exhibits the highest asphericity at $B/C \approx 0.90$. The presence of near-spherical charge distribution only in $B/C \approx 0.36$ suggests that the charge around Mg is being pulled more strongly along c direction (towards (0001) basal plane), than in the other nanocomposites, to attain this sphericity (Fig. 3a). In fact, this is supported by the electron richness in the (0001) basal plane in $B/C \approx 0.36$ as indicated by the positive $\rho_{\text{Octahedral}}/\rho_{\text{max}}$ (Fig. 3b, Supplementary Fig. S3). Further, it can also be observed from Fig. 3a that the electron density around Mg atom in $B/C \approx 0.36$ is the highest ($\sim 13.671 \text{ \AA}^{-3}$) among all the nanocomposites from the colour-coded scale. This shows that the various interactions in $B/C \approx 0.36$ are happening to a different extent compared with the other nanocomposites.

The different extent of the atomic interactions in $B/C \approx 0.36$ are evident from the increase in the Mg-C and B-C binding energies with respect to those in the lower compositions in the C-1s spectrum (Fig. 4a). This increase in the binding energies clearly indicates that a lower charge is received by C from both Mg and B³⁴. Moreover, the lower charge reception by C is reinforced by the absence of the C-2p $\pi \rightarrow \pi^*$ transition peak (Fig. 4a). An important question here is that: why does the charge reception by C decrease despite the charge donation by both Mg and B? The changes in the interactions of C with Mg and B also introduce observable interactions between Mg and B. Figure 4b shows the presence of Mg-B peak at

~51.3 eV, corresponding to the charge transfer from Mg to B³⁶. The combined analysis of C-1s and Mg-2p spectra (Fig. 4) clearly indicates that Mg is donating charge to both C and B. As a result of this, the net charge received by C from Mg decreases (Fig. 4a). Similarly, as B shares its valence electrons with Mg, lower net charge is received by C from B (Fig. 4a). The presence of both Mg-B and B-C interactions render B a charge acceptor (from Mg) and a donor (to C), respectively. However, the electron richness at octahedral sites, which B is likely occupying, suggests that B is negatively charged making it a net charge acceptor. The results clearly indicated that ternary Mg-B-C interactions develop in $B/C \approx 0.36$. Similar interactions are observed in the case of $B/C \approx 0.90$ (Fig. 4).

The nanocomposite with $B/C \approx 0.90$ exhibits similar lattice parameters as those of $B/C=0$ and $B/C \approx 0.36$ (Fig. 2) and asphericity close to that of $B/C=0$ (Fig. 3a). Its $\rho_{\text{Octahedral}}/\rho_{\text{max}}$ value is negative similar to those of $B/C=0$ and $B/C \approx 0.09$ (Fig. 3b, Supplementary Fig. S3). Despite these similarities, it shows longer incubation time (Fig. 1) for H-uptake. This suggests that, possibly, a different level of interactions is present in this nanocomposite. From Fig. 4, all the peaks (Mg-C, B-C and Mg-B) are shifted to lower binding energies compared with those in $B/C \approx 0.36$ suggesting stronger interactions similar to those in of MgB_2 ⁴⁵. However, the XRD pattern (Supplementary Fig. S1) does not show any MgB_2 peaks [ICSD code: 26675]. Moreover, the absence of a peak at ~188.5 eV in the B-1s spectra (Supplementary Fig. S5) suggests that B is not arranged in hexagonal structure which is necessary for the formation of MgB_2 ⁴⁵.

The analysis from the present study is used to propose a mechanism in terms of the structural and local environmental changes that help in reducing the incubation time during H-uptake. This mechanism is schematically shown in Fig. 5. Among the investigated compositions, those at $B/C > 0.09$ develop ternary Mg-B-C atomic interactions, where C from erGO receives charge from both Mg and B (Mg-C, B-C in Fig. 4a). Interestingly, B also receives charge from Mg developing Mg-B interactions (Fig. 4b). Such a charge reception renders B negative making it a net charge acceptor. This is evidenced by the electron-rich octahedral interstices in Mg unit cell, where there is a likelihood of B's presence (Fig. 3b, Supplementary Fig. S3). The attraction between the negatively charged B and Mg helps in maintaining the Mg unit cell size almost the same as that when B is absent (Fig. 2). Despite the charge donation to both C and B, the charge on Mg is $< +2$ rendering it difficult to bond with H (dotted arrow from H to Mg, Fig. 5). This results in the longer incubation times at $B/C > 0.09$ (Fig. 1).

At the critical ratio of $B/C \approx 0.09$, B acts as a charge donor to C (Fig. 4a). The presence of the positively charged B in the octahedral interstices of Mg unit cell ($\rho_{\text{Octahedral}}/\rho_{\text{max}}$, Fig. 3b, Supplementary Fig. S3) repels Mg ('repulsion', Fig. 5) and causes the lattice expansion (Fig. 2). Here, Mg is more positive relative to that at $B/C > 0.09$ due to the lower binding energy of Mg-C (Fig. 4a) rendering Mg-H bond stronger (solid arrow from H to Mg, Fig. 5) than in $B/C > 0.09$. The more positive Mg can bond strongly with H and can reduce the incubation time (Fig. 1).

The present study shows that various interactions among Mg, B and C in the Mg-B-erGO nanocomposites influence the reduction of incubation time and increase in the H-uptake kinetics in the order: (Mg→C; B→C) _{$B/C \approx 0.09$} > (Mg→C) _{$B/C=0$} > (ternary Mg→B→C) _{$B/C > 0.09$} .

Methods

Electrochemically reduced graphene oxide (erGO) was synthesized by electrochemical exfoliation of graphite rod (ϕ : 305 mm) using CHI 660E electrochemical work station in 0.1 M $(\text{NH}_4)_2\text{SO}_4$ aqueous electrolyte. Platinum mesh and Ag/AgCl (3 M KCl) were used as counter and reference electrodes, respectively. Potentiostatic exfoliation at 3 V for 3 h resulted in exfoliation of graphene sheets from the surface of graphite rod because of $(\text{SO}_4)^{2-}$ ion intercalation⁴⁶.

Magnesium (Sigma Aldrich; $\sim 44 \mu\text{m}$; $>99\%$), amorphous boron powder (Sigma Aldrich; $\leq 1 \mu\text{m}$; $>95\%$) were used along with erGO for synthesizing Mg-B-erGO nanocomposites. Four different nanocomposites with *B/C* weight ratios of 0, ~ 0.09 , ~ 0.36 and ~ 0.90 were synthesized. The corresponding *B/Mg* weight ratios are 0, ~ 0.01 , ~ 0.04 and ~ 0.10 , respectively. The erGO is always 10 wt % with respect to the total weight of the nanocomposite. All the samples in the present study are referred with respect to their *B/C* weight ratios to understand the synergetic effect of the catalysts B and C on H-uptake by Mg. All the materials were handled in argon atmosphere using MBraun Unilab Plus 4-port glovebox maintaining oxygen (O_2) and moisture (H_2O) levels at <0.1 ppm. The Mg-B-erGO nanocomposites were synthesized through ball milling by loading Mg, B and erGO in appropriate compositions into a 45 ml tungsten carbide (WC) vessel containing WC balls maintaining a ball to powder weight ratio of 40:1. A Fritsch pulverisette 7, premium line planetary micro mill was employed for ball milling.

Following ball milling the nanocomposites were loaded and sealed in a hydrogenation reactor inside glovebox. Subsequently, the reactor was brought out for H-uptake experiments in a Sievert's type apparatus. Prior to H-uptake, the reactor was purged with Ar. The reactor containing the powder was heated up to ~ 320 °C under vacuum. Eventually, hydrogen gas (99.999 %) was permitted in to the reactor at ~ 15 bar and ~ 320 °C. Isothermal H-uptake experiments were conducted on these Mg-B-erGO nanocomposites at these conditions up to saturation. The quantity of H-uptake by the powders was estimated using the ideal gas law²⁰.

The phase analysis on these nanocomposite powders was performed by X-ray diffraction (XRD) employing PANalytical EMPYREAN goniometer. Cu K α radiation (wave length: 1.5406 Å) was used for the same. The baseline correction was performed on the obtained data and the phases were indexed using the standard ICSD references. The ICSD database codes used for indexing Mg, MgO and rGO phases are 76748, 104845 and 31170, respectively.

The XRD patterns of the nanocomposites were subjected to Rietveld refinement using FullProf suite (version: 7.20) to estimate phase percentages and to obtain crystallographic data of phases²². Baseline for the experimentally obtained data was corrected using winPLOT program⁴⁷. After baseline correction, the data was refined using Pseudo-Voigt function⁴⁸. The lattice parameters (a , b , c , α , β , γ) of hcp Mg, FWHM (U , V , W , IG), shape (η_0 , X) and asymmetry were refined to obtain the best fit with the experimental data for Mg and MgO phases. For refining the lattice parameters, the initial values of $a = 3.2093$ Å, $b = 3.2093$ Å and $c = 5.2103$ Å were fed as input into EdPCR application of the FullProf suite prior to Rietveld

refinement. The electron density maps are used to estimate the local environment within the crystal lattice. Electron density maps for Mg unit cell were developed using GFourier Program (version: 4.06) through Maximum Entropy Method (MEM)²⁵. Through MEM the electron density $\rho(r)$ was calculated by Fourier transformation of structure factors obtained after Rietveld refinement⁴⁹.

X-ray photoelectron spectroscopy (XPS) was performed on the nanocomposites employing Axis Supra Photoelectron spectrometer (Kratos Analytical) using Al K α source. The powders were ultrasonicated in toluene for uniform dispersion following which they were drop casted onto Al foil and exposed to XPS source maintaining 20 eV pass energy. The obtained high resolution XPS spectra for various orbitals were deconvoluted using Gaussian function for estimating the chemical bonds²⁷.

Declarations

ACKNOWLEDGEMENTS

Financial support from Science and Engineering Research Board, Department of Science and Technology (Sanction Order number: EMR/2016/004969), India is appreciated. XRD by Department of Metallurgical Engineering and Materials Science, XPS by Central Surface Analytical Facility (ESCA Lab) at IIT Bombay are acknowledged.

Author information

Affiliations

Department of Energy Science and Engineering, Indian Institute of Technology Bombay, Mumbai-400076, India

Marla V V Satya Aditya

Srikanta Panda

Sankara Sarma V Tatiparti*

Contributions

Marla V V Satya Aditya: Experimental work, Data analysis and Interpretation, Designing Figures, Writing manuscript

Srikanta Panda: Experimental work, Data analysis and Interpretation

Sankara Sarma V Tatiparti: Research organization and supervision, Data analysis and Interpretation, Designing Figures, Writing manuscript

Corresponding author

Ethics declarations

Competing interests

The authors declare that they have no competing interests.

References

1. Schlapbach, L. & Züttel, A. Hydrogen-storage materials for mobile applications. *Nature***414**, 353–358 (2001).
2. Schneemann, A. *et al.* Nanostructured metal hydrides for hydrogen storage. *Chem. Rev.***118**, 10775–10839 (2018).
3. Jain, I. P., Lal, C. & Jain, A. Hydrogen storage in Mg: A most promising material. *Int. J. Hydrogen Energy***35**, 5133–5144 (2010).
4. Zaluska, A., Zaluski, L. & Ström-Olsen, J. O. Nanocrystalline magnesium for hydrogen storage. *J. Alloys Compd.***288**, 217–225 (1999).
5. Berube, V., Radtke, G., Dresselhaus, M. & Chen, G. Size effects on the hydrogen storage properties of nanostructured metal hydrides: A review. *Int. J. Energy Res.***31**, 637–663 (2007).
6. Wagemans, R. W. P., Van Lenthe, J. H., De Jongh, P. E., Van Dillen, A. J. & De Jong, K. P. Hydrogen storage in magnesium clusters: Quantum chemical study. *J. Am. Chem. Soc.***127**, 16675–16680 (2005).
7. Huot, J., Liang, G., Boily, S., Van Neste, A. & Schulz, R. Structural study and hydrogen sorption kinetics of ball-milled magnesium hydride. *J. Alloys Compd.***293**, 495–500 (1999).
8. Nagar, R., Vinayan, B. P., Samantaray, S. S. & Ramaprabhu, S. Recent advances in hydrogen storage using catalytically and chemically modified graphene nanocomposites. *J. Mater. Chem.***A5**, 22897–22912 (2017).
9. Cho, E. S. *et al.* Graphene oxide/metal nanocrystal multilaminates as the atomic limit for safe and selective hydrogen storage. *Nat. Commun.***7**, 1–8 (2016).
10. Liu, G., Wang, Y., Jiao, L. & Yuan, H. Understanding the role of few-layer graphene nanosheets in enhancing the hydrogen sorption kinetics of magnesium hydride. *ACS Appl. Mater. Interfaces***6**, 11038–11046 (2014).
11. Yan, Y., Remhof, A., Rentsch, D. & Züttel, A. The role of $\text{MgB}_{12}\text{H}_{12}$ in the hydrogen desorption process of $\text{Mg}(\text{BH}_4)_2$. *Chem. Commun.***51**, 700–702 (2015).
12. Kou, H.-Q., Xiao, X.-Z., Chen, L.-X., Li, S.-Q. & Wang, Q.-D. Formation mechanism of MgB_2 in $2\text{LiBH}_4 + \text{MgH}_2$ system for reversible hydrogen storage. *Trans. Nonferrous Met. Soc. China***21**, 1040–1046 (2011).

13. Kurko, S., Mamula, B. P., Rmuš, J., Novaković, J. G. & Novaković, N. DFT study of boron doped MgH₂: Bonding mechanism, hydrogen diffusion and desorption. *Int. J. Hydrogen Energy***45**, 7947–7957 (2020).
14. Liu, Y.-S. *et al.* Nanoscale Mg–B via Surfactant Ball Milling of MgB₂: Morphology, composition, and improved hydrogen storage properties. *J. Phys. Chem. C***124**, 21761–21771 (2020).
15. Nachimuthu, S., Lai, P., Leggesse, E. G. & Jiang, J. A first principles study on boron-doped graphene decorated by Ni-Ti-Mg atoms for enhanced hydrogen storage performance. *Sci. Rep.***5**, 1–8 (2015).
16. Boateng, E., Dondapati, J. S., Thirupathi, A. R. & Chen, A. Significant enhancement of the electrochemical hydrogen uptake of reduced graphene oxide via boron-doping and decoration with Pd nanoparticles. *Int. J. Hydrogen Energy***45**, 28951–28963 (2020).
17. Zhang, J., Xia, G., Guo, Z. & Zhou, D. Synergetic effects toward catalysis and confinement of magnesium hydride on modified graphene: A first-principles study. *J. Phys. Chem. C***121**, 18401–18411 (2017).
18. Shrinivasan, S., Kar, T., Neergat, M. & Tatiparti, S. S. V. Mg-C interaction induced hydrogen uptake and enhanced hydrogen release kinetics in MgH₂-rGO nanocomposites. *J. Phys. Chem. C***122**, 22389–22396 (2018).
19. Muthu, R. N. & Tatiparti, S. S. V. Electrode and symmetric supercapacitor device performance of boron-incorporated reduced graphene oxide synthesized by electrochemical exfoliation. *Energy Storage***2**, e134 (2020).
20. Gangrade, A. S., Varma, A. A., Gor, N. K., Shrinivasan, S. & Tatiparti, S. S. V. The dehydrogenation mechanism during the incubation period in nanocrystalline MgH₂. *Phys. Chem. Chem. Phys.***19**, 6677–6687 (2017).
21. Mondal, O. *et al.* Reduced graphene oxide synthesis by high energy ball milling. *Mater. Chem. Phys.***161**, 123–129 (2015).
22. Rodriguez-Carvajal, J. FULLPROF, a program for Rietveld refinement and pattern matching analyses. *Satellite Meeting on Powder Diffraction of the XVth Congress of the International Union of Crystallography* **127**, (1990).
23. Scherrer, P. Nachr Ges wiss goettingen. *Math. Phys.***2**, 98–100 (1918).
24. Kittel, C., McEuen, P. & McEuen, P. *Introduction to solid state physics.* **8**, (Wiley New York, 1996).
25. Gull, S. F. & Daniell, G. J. Image reconstruction from incomplete and noisy data. *Nature***272**, 686–690 (1978).
26. Pozzo, M. & Alfè, D. Hydrogen dissociation and diffusion on transition metal (= Ti, Zr, V, Fe, Ru, Co, Rh, Ni, Pd, Cu, Ag)-doped Mg(0001) surfaces. *Int. J. Hydrogen Energy***34**, 1922–1930 (2009).
27. Koenig, M. F. & Grant, J. T. Deconvolution in X-ray photoelectron spectroscopy. *J. Electron Spectros. Relat. Phenomena***33**, 9–22 (1984).
28. Wang, Y., Wang, C., Wang, Y., Liu, H. & Huang, Z. Boric acid assisted reduction of graphene oxide: a promising material for sodium-ion batteries. *ACS Appl. Mater. Interfaces***8**, 18860–18866 (2016).

29. Li, S. *et al.* Plasma-induced highly efficient synthesis of boron doped reduced graphene oxide for supercapacitors. *Chem. Commun.***52**, 10988–10991 (2016).
30. Rabchinskii, M. K. *et al.* From graphene oxide towards aminated graphene: facile synthesis, its structure and electronic properties. *Sci. Rep.***10**, 1–12 (2020).
31. Kovtun, A. *et al.* Accurate chemical analysis of oxygenated graphene-based materials using X-ray photoelectron spectroscopy. *Carbon***143**, 268–275 (2019).
32. Rana, K. *et al.* Analysis of Charge Transfer for in situ Li intercalated carbon nanotubes. *J. Phys. Chem. C***116**, 11364–11369 (2012).
33. Zhang, T., Song, W., Kou, H. & Li, J. Surface valence transformation during thermal activation and hydrogenation thermodynamics of Mg-Ni-Y melt-spun ribbons. *Appl. Surf. Sci.***371**, 35–43 (2016).
34. Van der Heide, P. *X-ray photoelectron spectroscopy: an introduction to principles and practices.* (John Wiley & Sons, 2011).
35. Chen, J. L. & Zhu, J. H. A query on the Mg 2p binding energy of MgO. *Res. Chem. Intermed.***45**, 947–950 (2019).
36. Talapatra, A. *et al.* X-ray photoelectron spectroscopy studies of MgB₂ for valence state of Mg. *Phys. C Supercond. its Appl.***419**, 141–147 (2005).
37. Kawamura, R. *et al.* Photoinduced hydrogen release from hydrogen boride sheets. *Nat. Commun.***10**, 1–8 (2019).
38. Vajeeston, P. *et al.* Structural stability and pressure-induced phase transitions in MgH₂. *Phys. Rev. B***73**, 224102 (2006).
39. Tesch, J., Voloshina, E., Fonin, M. & Dedkov, Y. Growth and electronic structure of graphene on semiconducting Ge(110). *Carbon***122**, 428–433 (2017).
40. Huang, L. F. *et al.* Modulation of the thermodynamic, kinetic, and magnetic properties of the hydrogen monomer on graphene by charge doping. *J. Chem. Phys.***135**, 064705 (2011).
41. Allred, A. L. & Rochow, E. G. A scale of electronegativity based on electrostatic force. *J. Inorg. Nucl. Chem.***5**, 264–268 (1958).
42. Kobayashi, S., Ikuhara, Y. & Mizoguchi, T. Lattice expansion and local lattice distortion in Nb- and La-doped SrTiO₃ single crystals investigated by x-ray diffraction and first-principles calculations. *Phys. Rev. B***98**, 134114 (2018).
43. Wu, Z., Zhu, L., Yang, F., Jiang, Z. & Zhang, Z. First-principles insights into influencing mechanisms of metalloid B on Mg-based hydrides. *J. Alloys Compd.***693**, 979–988 (2017).
44. Wang, G. *et al.* Interlayer coupling behaviors of boron doped multilayer graphene. *J. Phys. Chem. C***121**, 26034–26043 (2017).
45. Matera, D. *et al.* High-field superconductivity in C-doped MgB₂ bulk samples prepared by a rapid synthesis route. *Sci. Rep.***10**, 1–16 (2020).
46. Parvez, K. *et al.* Exfoliation of graphite into graphene in aqueous solutions of inorganic salts. *J. Am. Chem. Soc.***136**, 6083–6091 (2014).

47. Roisnel, T. & Rodríguez-Carvajal, J. WinPLOTR: a windows tool for powder diffraction pattern analysis. in *Materials Science Forum***378**, 118–123 (2001).
48. Young, R. A. & Wiles, D. B. Profile shape functions in Rietveld refinements. *J. Appl. Crystallogr.***15**, 430–438 (1982).
49. Smaalen, S. Van & Netzel, J. The maximum entropy method in accurate charge-density studies. *Phys. Scr.***79**, 048304 (2009).

Figures

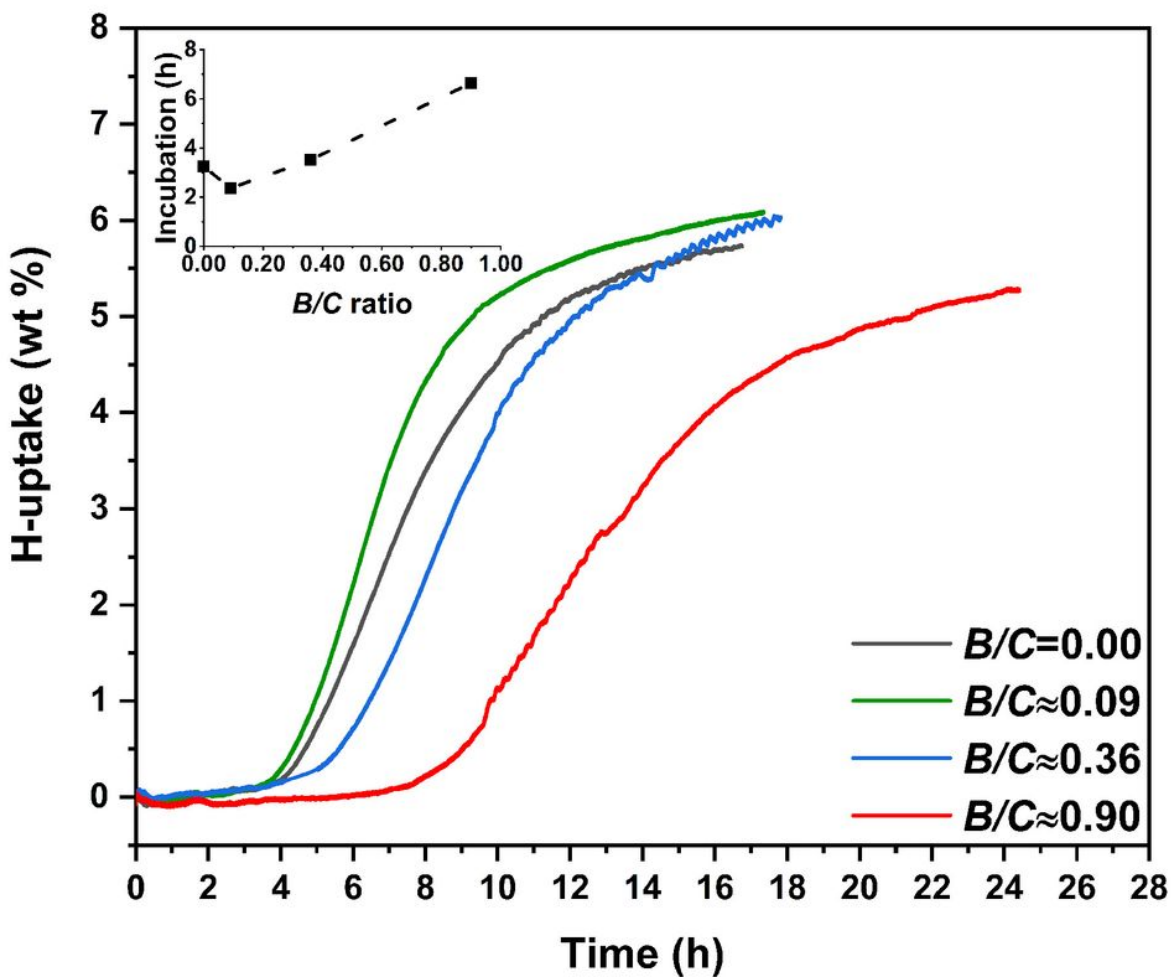


Figure 1

H-uptake (wt %) versus time (h) in ball milled Mg-B-erGO nanocomposites at various B/C ratios obtained at ~15 bar, ~320 °C. Inset shows the incubation (h) plotted against B/C ratio.

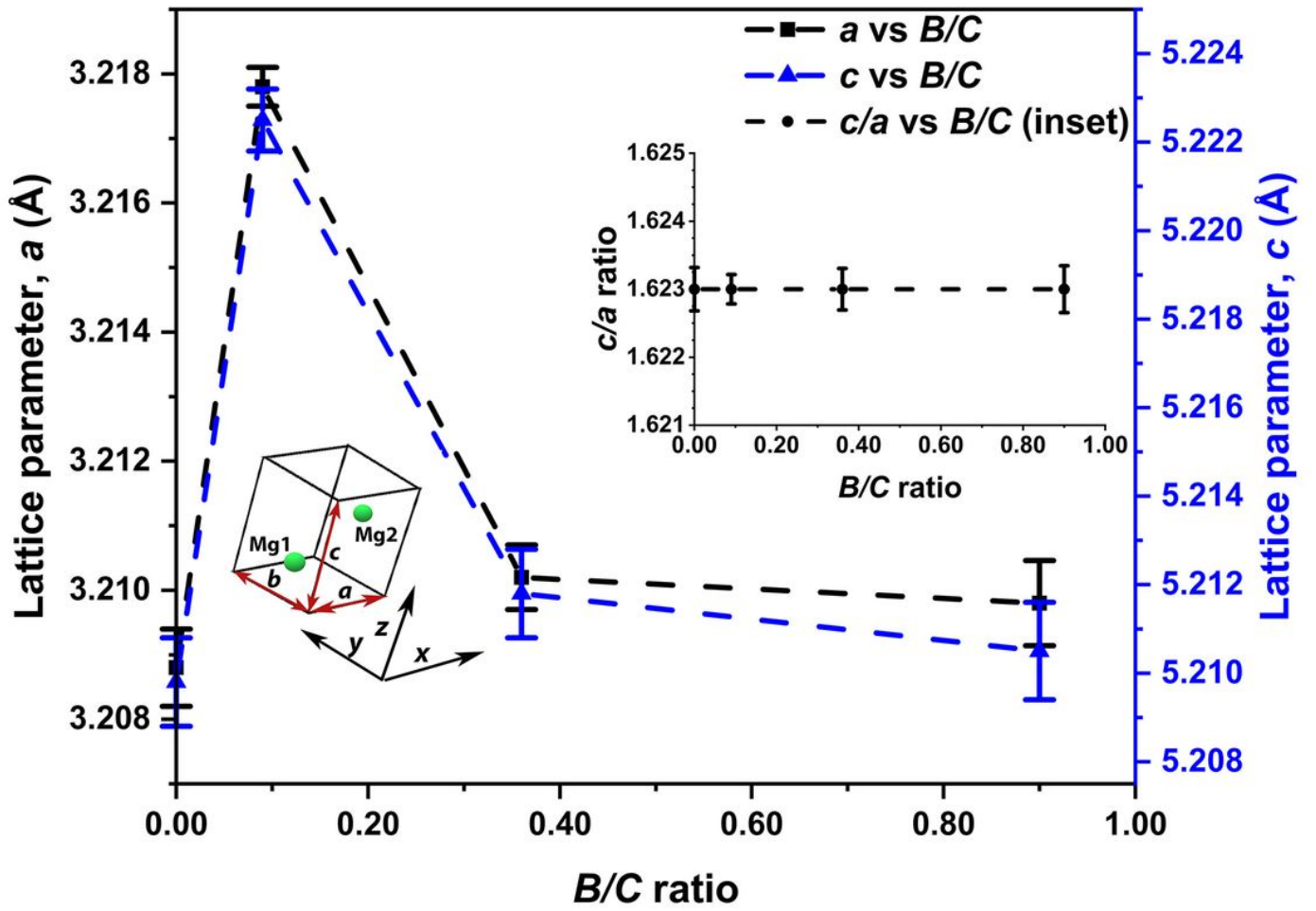


Figure 2

Lattice parameters of Mg (hcp) versus B/C ratio in ball milled Mg-B-erGO nanocomposites.

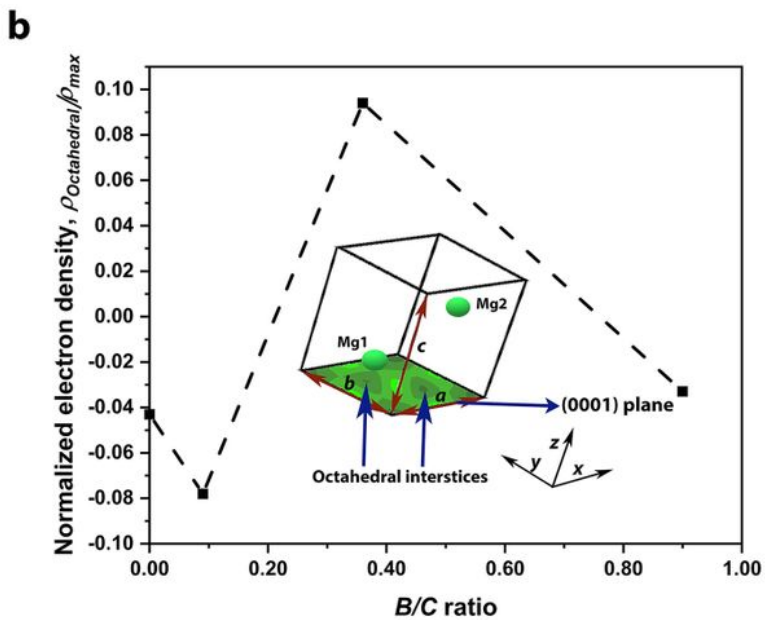
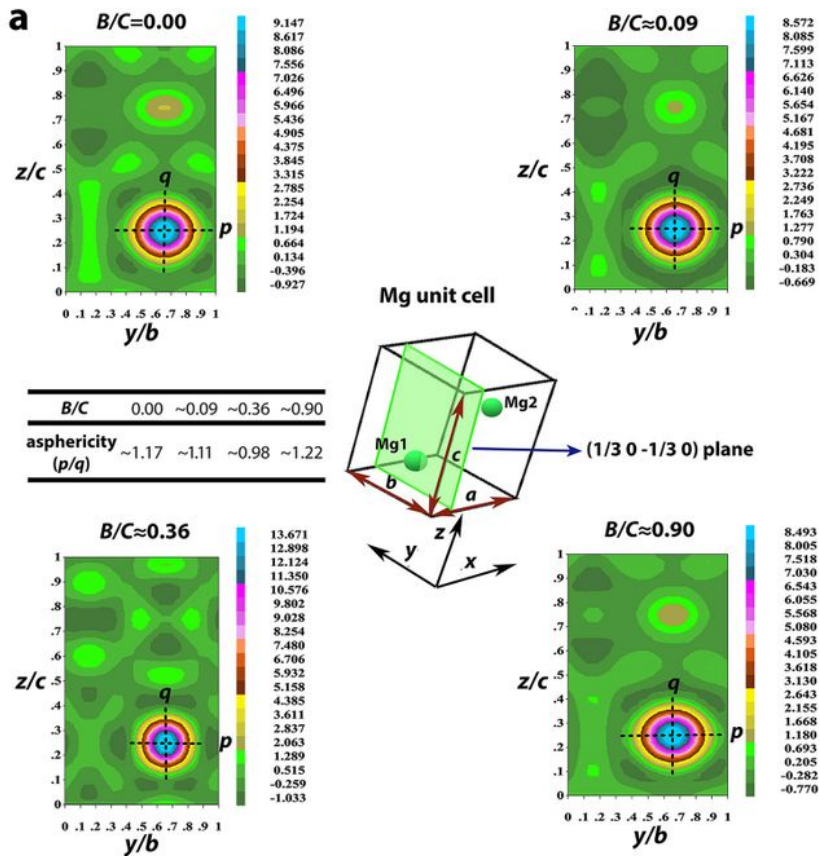


Figure 3

(a) Electron density maps corresponding to Mg $(1/3\ 0\ -1/3\ 0)$ plane and asphericity (p/q) of charge distribution around Mg1 atom at various B/C ratios; (b) Normalized electron density ($\rho_{\text{Octahedral}}/\rho_{\text{max}}$) at octahedral sites in Mg (0001) plane plotted against B/C ratio for ball milled Mg-B-erGO nanocomposites.

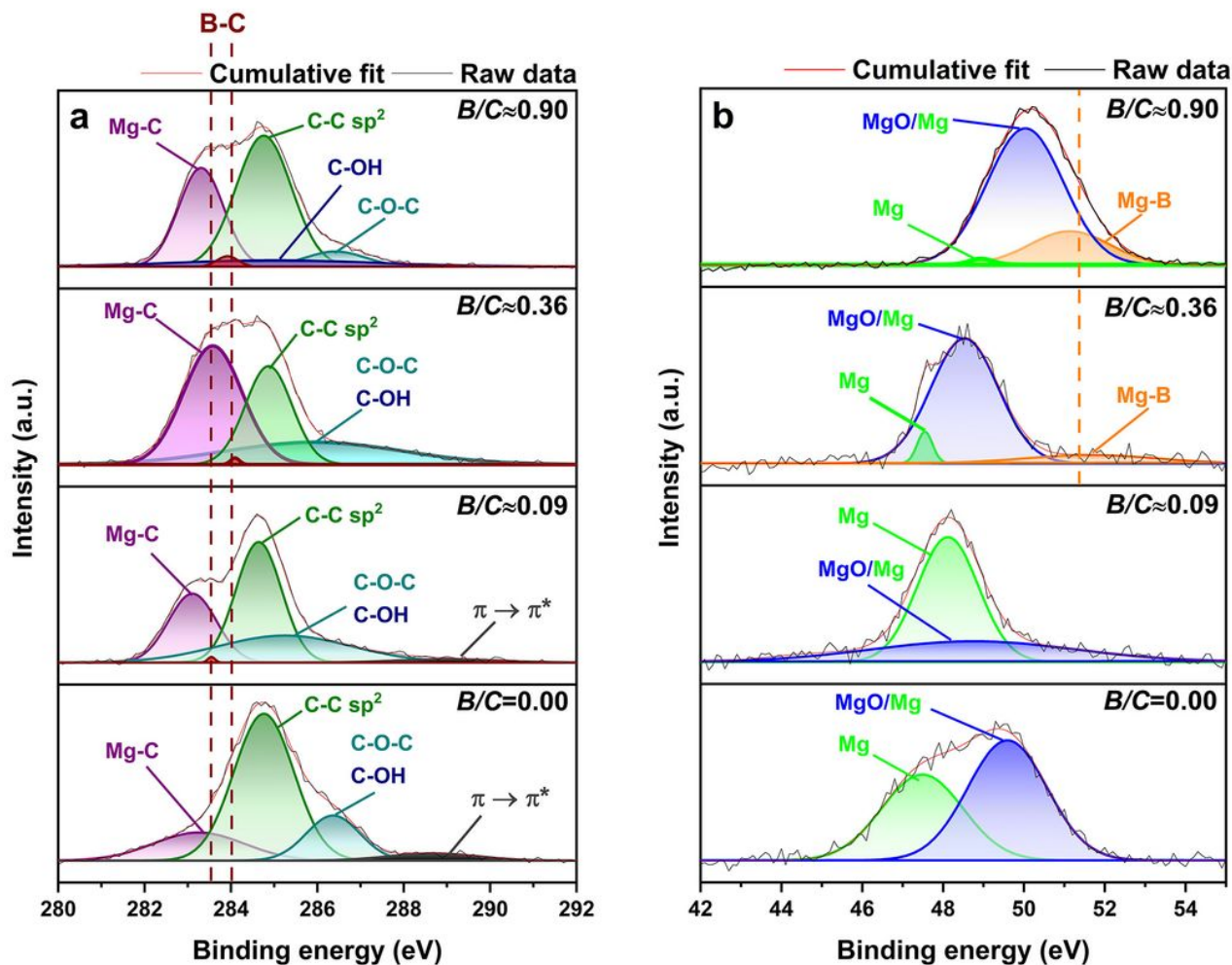


Figure 4

(a) C-1s core XPS spectra deconvoluted into Mg-C, B-C, sp² hybridized C-C, C-OH, C-O-C and C-2p $\pi \rightarrow \pi^*$ transition peaks; (b) Mg-2p spectra deconvoluted into metallic Mg, MgO and Mg-B for all the ball milled Mg-B-erGO nanocomposites.

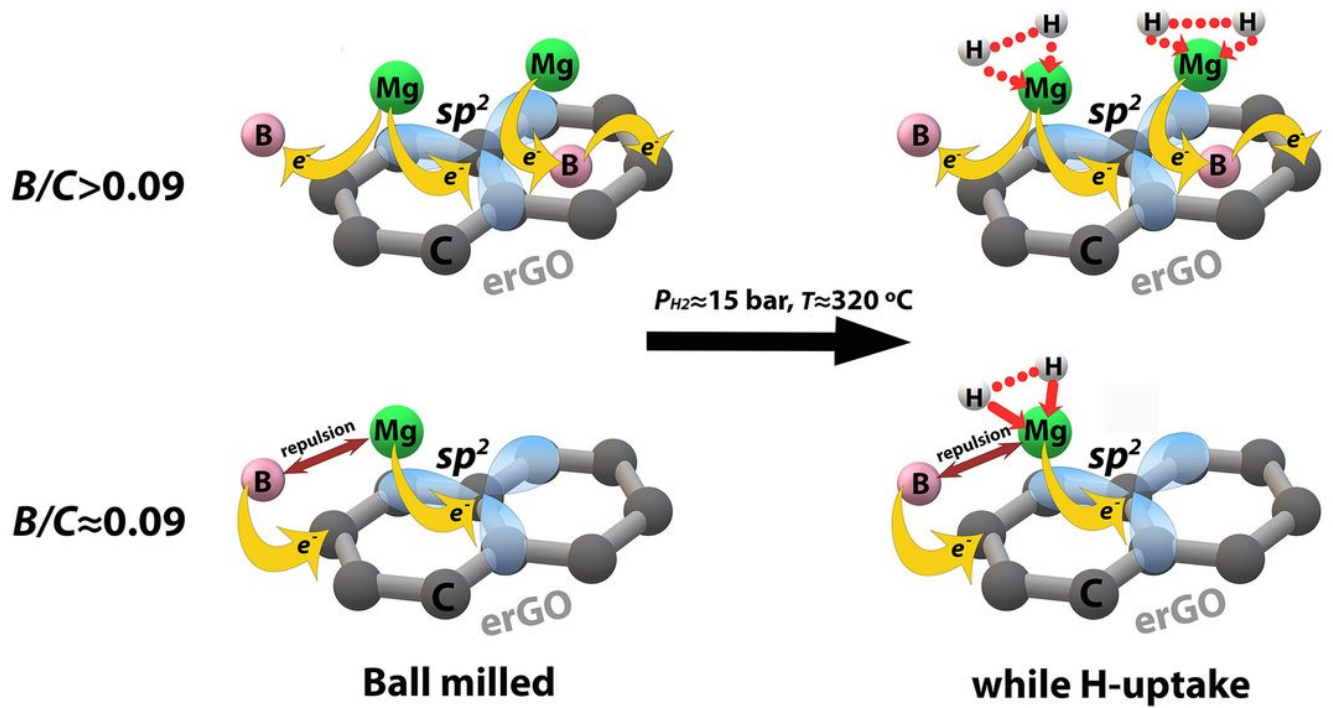


Figure 5

Various interactions among Mg, B, C at $B/C > 0.09$ and ~ 0.09 in Mg-B-erGO nanocomposites after ball milling and while H₂-uptake.

Supplementary Files

This is a list of supplementary files associated with this preprint. Click to download.

- [Supplementaryinformation.pdf](#)